Contents lists available at ScienceDirect

Journal of Photochemistry & Photobiology, A: Chemistry

journal homepage: www.elsevier.com/locate/jphotochem

SrNiO$_3$ perovskite/CeO$_2$ composites as heterogeneous photocatalysts for the 2-propanol oxidation in gas–solid regime

N. Aoun [a,b], E.I. García-López [c,*], H. Boucheloukh [b,d], M. Boulekroune [e], T. Sehili [d], G. Marcì [a]

[a] Università di Palermo, Dipartimento di Ingegneria, Viale delle Scienze Ed. 6, 90128 Palermo, Italy
[b] Department of Chemistry, Faculty of Exact Sciences and Informatics, University of Jijel, 18000 Jijel, Algeria
[c] Università di Palermo, STEBICEF, Viale delle Scienze Ed. 16, 90128 Palermo, Italy
[d] Laboratory of Sciences and Technologies of the Environment University of Constantine I, 25000 Constantine, Algeria
[e] Environmental and Structural Molecular Chemistry Research Unit (UR-CHEMS), Faculty of Exact Sciences, University of Constantine 1, 25000, Algeria

A B S T R A C T

Both SrNiO$_3$ perovskite and CeO$_2$ are materials suitable for photocatalytic purposes. In this work, the preparation and physicochemical characterization of bare SrNiO$_3$ and CeO$_2$ along with composites where CeO$_2$ was enriched with the perovskite from 15 to 70 % in mass of SrNiO$_3$ in the composite are described. The materials have been used for the photocatalytic oxidation of 2-propanol in gas–solid regime in the presence of UV-LED or simulated solar irradiation. The solids were characterized by XRD, SEM/EDX, N$_2$ adsorption/desorption and FTIR and UV–Vis diffuse reflectance spectroscopies. The composite containing 15 % w/w of SrNiO$_3$ and 85 % w/w of CeO$_2$ resulted the most active, giving rise the complete degradation of 2-propanol after 1.5 h or 6.0 h of irradiation by UV-LED and simulated solar light irradiation, respectively. Photocatalytic activity results are discussed considering the physical–chemical properties on the catalysts.

1. Introduction

Heterogeneous photocatalysis is a technology extensively applied in the framework of environmental remediation. It requires the use of solid semiconductor that can accelerate the reaction rate and increase the efficiency of the process with the aid of light as radiation source [1]. The development of new and efficient photocatalysts is, therefore, crucial for advancing in the sustainability of the technology in the pursuit of clean, inexpensive, and efficient technologies for environmental purposes. In this context, perovskites are materials with a unique crystal structure that have been extensively studied in solar cells, LEDs, sensors, energy, and catalysis fields.

A perovskite is represented by the general formula ABX$_3$, where A, B and X sites are an alkaline-earth or rare-earth metal cation with large atomic radii, transition-metal cation (e.g., Ti, Fe, Co, Mn and Ni) with the small atomic radii and an anion (e.g., O, S, N, and halides), respectively. Their crystal structure consists of a cubic unit cell with a central metal cation surrounded by oxygen atoms in an octahedral arrangement. Cations of A and B are combined with X anions by 12- and 6-fold coordination, respectively (See Fig. 1). Substitution of A-, B- and X-sites by the different valences and atomic radii generates the distorted structure of perovskite, which exhibits various physical–chemical traits such as oxygen vacancies, excellent thermal stability, superior electronic conductivity, and redox active sites. Consequently, they have received significant attention in the field of catalysis [2] and photocatalysis [3,4].

The most studied perovskites include metal oxides-based perovskites active as heterogeneous photocatalysts due to their high surface area and excellent charge transfer properties (some examples of this kind of perovskite are: LaFeO$_3$, SrTiO$_3$, and CaTiO$_3$. Another type of perovskite are the metal halide-based ones which are hybrid perovskites containing both inorganic and organic components studied for their high efficiency in solar cells [5]. Finally, a further class of perovskite is represented by double perovskites that contain two different metal cations in the B site, which results in unique properties such as a tuneable bandgap and improved stability. Two examples of these last materials are Sr$_2$FeMoO$_6$ and Ba$_2$BiIrO$_6$ [6].

Among the metal oxides-based perovskites strontium nickelate (SrNiO$_3$) has been studied very few, much less than other perovskites, and it has been proved to be active in water photo-splitting [7] and CO$_2$ reduction [8]. As far as we know only one paper has been devoted to the study of the photocatalytic degradation of pollutants by using SrNiO$_3$ in liquid–solid regime [9] but no research has been devoted to the study of
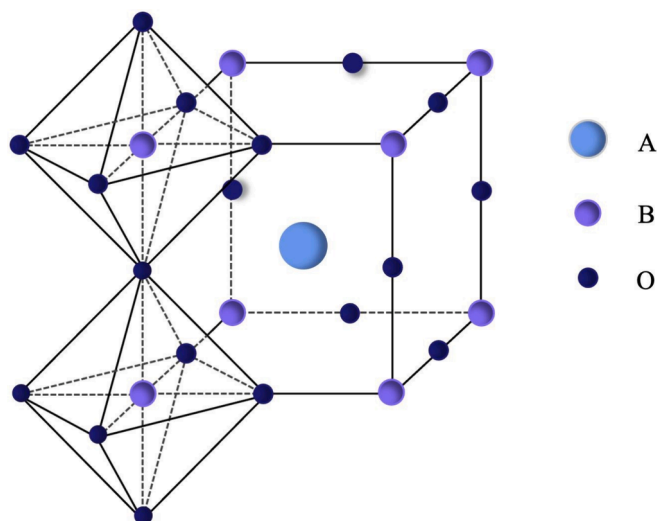
Fig. 1. Scheme of the structure of the ABX$_3$ perovskite type oxides.

a photocatalytic oxidation reaction in gas–solid regime.

Rare-earth nickelates have been widely studied but few studies are reported on alkaline-earth nickelates and their electronic structure is under debate [10]. SrNiO$_3$ is characterized by the presence of Ni^{3+} ions with a d^7 partially filled electron configuration giving rise to an interesting semiconductor electronic structure to be used as photocatalyst. For a divalent A such as Sr^{2+}, in the absence of oxygen vacancies, ANiO$_3$ would require a formal valence of Ni^{4+}. Several methodologies have been developed for the synthesis of SrNiO$_3$ influencing its physical–chemical features including solid-state reaction, sol–gel, hydrothermal, and microwave-assisted methods. There have been several studies of bulk hexagonal nickelates with divalent A such as SrNiO$_3$ [11,13] and BaNiO$_3$. [12] Hexagonal SrNiO$_3$ has been synthesized by calcination [13] or by heating under oxygen pressure in the range 50–2000 atm (whereas 1 atm oxygen produced SrNiO$_{2.5}$) [14]. SrNiO$_{2.5}$, Sr$_4$Ni$_3$O$_9$, Sr$_5$Ni$_4$O$_{11}$, and Sr$_9$Ni$_7$O$_{21}$ have also been synthesized [15].

Cerium oxide (CeO$_2$) has been also studied as photocatalyst, indeed due to its suitable band gap, excellent stability, cost-effectiveness, non-photo-corrosiveness, and low toxicity, ceria has been employed widely in photocatalysis [16]. It is a n-type semiconductor with a large band gap spanning from 2.6 to 3.4 eV, however due to its high electron hole recombination rate and poor capacity to absorb visible light, it performs poorly as a photocatalyst [17]. Composites of SrNiO$_3$ and CeNiO$_3$ were used for me-thane dry reforming for the generation of syngas [18]. In the current research, composites containing CeO$_2$ and the SrNiO$_3$ perovskite have been prepared. The purpose of this study is to illustrate the distinctive impact of SrNiO$_3$ and CeO$_2$ particle cohabitation in the photocatalytic oxidation of 2-propanol carried out in gas–solid regime under simulated solar light or UV-LED irradiation. The composite materials have been prepared with different mass ratio of the two components and the most active resulted that with 15 % of perovskite.

The photocatalytic oxidation of 2-propanol in gas–solid regime has been chosen as a model reaction because this molecule is a major contaminant in indoor air and air streams [19]. 2-propanol is a common volatile organic pollutant found in urban settings, especially indoor ones from items including waxes, varnishes, home goods, and building materials [20]. The use of 2-propanol as model molecule to study the activity of novel prepared photocatalysts in gas–solid regime is widely reported also because the photo-oxidation mechanism is well ascertained [21–23].

2. Materials and methods

2.1. Synthesis of photocatalysts

SrNiO$_3$ was synthesized via sol–gel method by the nitrate-citrate route [9] For that aim, strontium nitrate (0.02 mol of Sr(II)) and nickel nitrate hexahydrate (0.02 mol of Ni(II)) were dissolved in 100 mL of bidistilled water. Then 0.06 mol of citric acid, used as chelating agent, was added dropwise. The mixture was heated up to 80 °C and stirred for 3 h to obtain a green gel that was dried at 80 °C for 12 h and finally heated at 900 °C (ramp temperature of 5 °C•min^{-1}) and calcined for 5 h to obtain SrNiO$_3$ crystalline phase (labelled in the following as SNO). On the other hand, for the preparation of CeO$_2$ was followed a methodology already reported by some of us was [24]. An aqueous solution of Cerium nitrate (Ce(III) 0.01 M) was mixed with NH$_4$OH (0.04 M) solution (final pH 9) using magnetic stirring until a yellowish precipitate was formed. The precipitate was then filtered and dried at 80 °C overnight after being rinsed several times with bi-distilled water. The final product was calcined for 3 h at 600 °C.

The composites CeO$_2$/SNO were prepared using different mass ratio of CeO$_2$ and SrNiO$_3$ by a ball milling treatment. A RETSCH Planetary Ball Mill Model PM400 equipped with a ZrO$_2$ jar with 6 zirconium oxide balls with rotation speed of 150 rpm was used for 2 h. The composite powders were therefore calcined at 400 °C for 30 min. Composites possessing a nominal mass ratio SNO:CeO$_2$ equal to 15:85, 30:70, 50:50 and 70:30 were obtained; the solid composites were labelled as SNO-15, SNO-30, SNO-50 and SNO-70, respectively, where the number in the label correspond to the percentage of perovskite in the composite.

2.2. Characterization of photocatalysts

X-ray diffraction analysis was performed on a D8 advance diffractometer using Cu Kα radiation operating at 40 kV with a 0.02 degrees step. The average crystallite size was calculated using the Scherrer equation. Scanning electron microscopy (SEM) was performed by using a FEI Quanta 200 ESEM microscope, operating at 20 kV on specimens upon which a thin layer of gold had been evaporated. An electron microprobe used in an energy dispersive mode (EDX) was employed to obtain information on the actual metals' ratio present in the samples. Specific surface area, average pore volume and size were obtained with the help of a Micromeritics equipment (model, ASAP 2020) following nitrogen adsorption at 77 K and using the Brunauer-Emmett-Teller (BET) method. Samples were degassed under flowing argon at 473 K for 2 h before nitrogen adsorption. FTIR spectra in KBr pellets were obtained with a Shimadzu FTIR-8400 spectrometer (4 cm^{-1} resolution, 256 scans). Ultraviolet–visible diffuse reflection spectroscopy (DRS) was useful to calculate the band gaps of the samples. DRS spectra were recorded in the λ range 250–600 nm with a Shimadzu UV-2401 PC instrument with BaSO$_4$ as the reference sample. The spectra of the samples were carried out by using mixtures of the photocatalyst with BaSO$_4$ in a mass ratio of 0.050:1.

Electrochemical experiments aimed to understand the electronic properties of the semiconductor materials were carried out in 1 M KCl solution, using a Potentiostat/Galvanostat Gamry Reference 3000 with a three-electrode system. A saturated calomel electrode (SCE) was used as a reference electrode, Pt as a counter electrode, and SNO, CeO$_2$, SNO-15, SNO-30, SNO-50, SNO-70 as working electrodes. For this purpose each working electrode was prepared as 10 mm diameter pellet using uniaxial pressure of 10 MPa and sintered at 600 °C for 2 h. Finaly, it was introduced into resin epoxy, polished with SIC paper (1200) and washed with water, only one side of ca.1 cm^2 was in contact with the electrolyte. Painted silver lacquer was used to insure the electrical contact between the back pellet and copper wire. The electrochemical impedance spectroscopy (EIS) measurements were performed in the range of 0.1–10^5 Hz, with an AC voltage amplitude of 10 mV, at open circuit potential.

2.3. Photocatalytic oxidation of 2-propanol

The photoreactivity of the powders was studied in the gas–solid regime for the oxidation of 2-propanol. A 25 mL cylindrical Pyrex batch photoreactor (diameter 42 mm, height 18 mm) was employed introducing the photocatalyst powder (100 mg) dispersed in the bottom. Then O_2 was insufflated, and a saturated oxygen atmosphere was reached. Liquid 2-propanol was injected into the photoreactor (nominal initial concentration 1 mM) and irradiation was started only after steady state conditions were achieved, i.e. after ca. 30 min of dark stabilization conditions. The employed set-up is reported elsewhere [25]. The photoreactor was irradiated from the top by two different irradiation systems, i.e. a UV-LED IRIS 40 with an irradiation peak centred at 365 nm and a SolarBox apparatus (CO.FO.ME.GRA srl), provided with a 1500 W high pressure Xenon lamp simulating the solar light. The power of the light measured in the range 315–400 nm by a UVX Digital radiometer reaching the reactor resulted 630 or 14 mW, for the UV-LED and the SolarBox, respectively. The irradiate surface of the reactor was 1,380 mm^2.

For all experiments, irradiation started only after half hour of dark adsorption equilibrium of the substrate on the photocatalyst surface. The photocatalytic runs lasted two or six hours, in the presence of the UV-LED or SolarBox irradiation, respectively. Samples of the reacting fluid were analysed during the course of the reaction by withdrawing 250 μl of gas from the outlet of the reactor by means of a gas-tight syringe. The concentrations of 2-propanol and its reaction intermediates were determined by a Shimadzu 2010 gas chromatograph (GC) equipped with a Phenomenex Zebron Wax-plus and a FID detector using He as a carrier gas. The amount of CO_2 was, instead, analysed by a HP 6890 Series GC equipped with a packed column GC 60/80 Carboxen-1000 and a TCD.

Blank reactivity tests were performed under the same experimental conditions used for the photo-reactivity experiments but in the absence of catalyst, oxygen, or light. No reactivity was observed in all these cases, so it was concluded that the simultaneous presence of O_2, catalyst, and irradiation was needed for the occurrence of the 2-propanol degradation process.

3. Results and discussion

3.1. Bulk and surface physical–chemical characterization of the photocatalysts

XRD patterns of the CeO_2, $SrNiO_3$ and composites SNO-15, SNO-30, SNO-50, SNO-70 are reported in Fig. 2. CeO_2 shows the typical pattern attributed to the cubic fluorite-type structure JCPDS [99–101–0981] being, as reported before [26], most intense the Miller indices for the planes (1 1 1) and (2 0 0) located at 2θ = 28.5° and 33.1°, respectively. The unit cell is characterized by a = b = c = 5.41 Å with a cell volume Vcell ≈ 158 Å^3. The diffractogram of pristine $SrNiO_3$ shows peaks at 2θ at 29.6, 32.8; 38, 41.2, 44.7, 45.7, 46.4, 50.3, 56.5, 58.5, 60.9, 68.7, 75.4, and 76.4 degree. The XRD pattern corresponds to the JCPDS [00–033–1347], which refers to the hexagonal crystalline phase with cell parameters: a = 5.47, b = 5.47, c = 19.73 Å and Vcell ≈ 511 Å^3 as observed before by some of us [9]. These results are in agreement with previous reports where, as in this research, the $SrNiO_3$ was prepared by sol–gel method [18]. The corresponding unit cell parameters, and cell volume are provided in Table 1. The crystallographic parameters and particle size of the studied materials are calculated according to Debye Sheerer equation [27].

No peaks correspond to any other impurities and all the samples maintain a good degree of crystallinity, since their reflections appear still sharp and intense. The intensity of the main peak attributed to the $SrNiO_3$ hexagonal phase located at 2θ = 32.8° increased by increasing the amount of the perovskite in the series SNO-15, SNO-30, SNO-50 and SNO-70. It is worth to note that, for composite materials with the lower
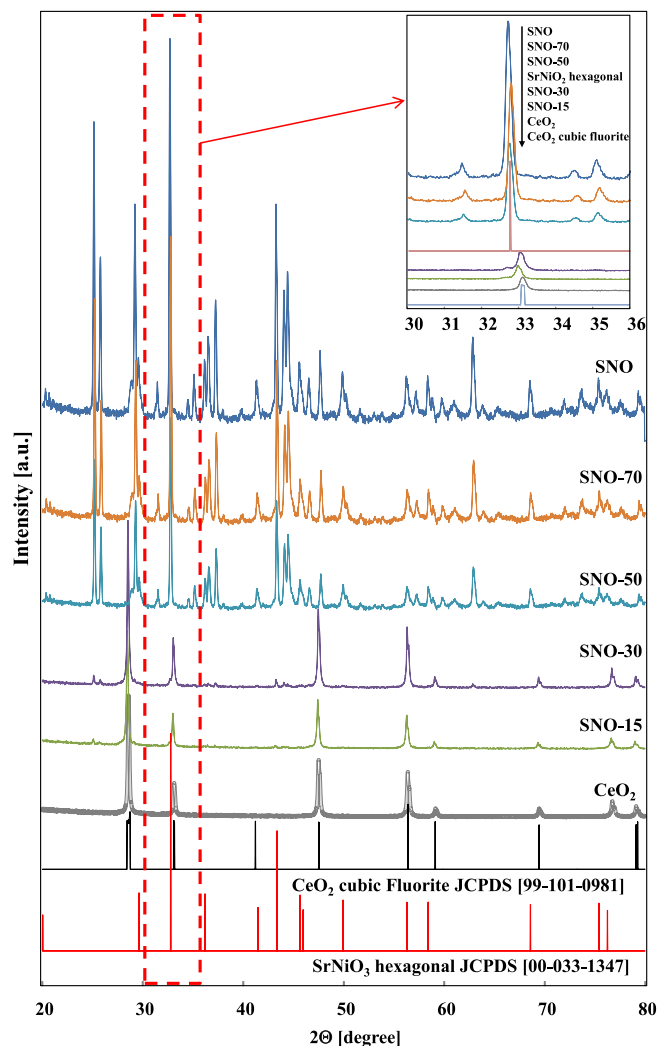

Fig. 2. XRD patterns of the pristine $SrNiO_3$ (SNO) and CeO_2 along with the composite photocatalysts.

Table 1
Crystallographic features of the photocatalytic materials.

Sample	Space group	Cell parameters (Å)			Cell volume (Å^3)	Particle size (Å)
		a	b	c		
SNO	Hexagonal	5.47	5.47	19.7	511	541
CeO_2	Cubic	5.41	5.41	5.41	158	536
SNO-15	Cubic	5.41	5.41	5.41	159	533
SNO-30	Cubic	5.41	5.41	5.41	159	530
SNO-50	Hexagonal	5.47	5.47	19.7	511	541
SNO-70	Hexagonal	5.87	5.87	19.80	513	541

amount of SNO this peak overlap with that characteristic of CeO_2 at 2θ = 33.1° where-as a clear peak shift versus 2θ = 32.8° is observed by increasing the amount of SNO in the composite. Indeed, as shown in the inset of Fig. 2, for SNO-50 and SNO-70 the diffraction peak appears at a 2θ value between 32.8 and 33.1° due to the contemporary and comparable diffraction of the crystallites of SNO and CeO_2 in the composites. On the other hand, the presence of a small diffraction band at ca. 32.7° observed for SNO-15 and SNO-30 (see inset of Fig. 2) evidences the presence of a distorted perovskite phase. This peak at 32.7 would be the result of a strong interaction between perovskite and ceria in these two

composites.

SEM microphotographs of the various samples are reported in Fig. 3. The morphology of the two bare samples SNO and CeO_2 are completely different as reported in Fig. 3 (a) and (b), respectively. Composites (Fig. 3 (c) to (f)) appear not so much homogeneous as also evidenced by the EDX analysis carried out on different spots on their surface. The average value of the percentage of Ni, Sr and Ce present in the samples corresponds to the nominal amounts even if some fluctuations of their values are observed depending on the area of the sample analysed. It is observed that the CeO_2 particles are coated by the SNO in the composites, even if in some cases it is possible to detect the presence of CeO_2 (see Fig. 3 (d) for the SNO-30 sample). The particle sizes of the composite samples appear smaller than those of both pristine CeO_2 and $SrNiO_3$, and this fact can be attributed to the ball milling treatment used for the preparation of these materials.

Table 2 summarizes for all the prepared samples the Brunauer-Emmett-Teller (BET) specific surface area (SSA) and the porosity parameters that were determined by the nitrogen adsorption–desorption isotherms reported in Fig. 4. From the perusal of Table 2 the SSA of the composite materials decreases by increasing the perovskite amount (from SNO-15 to SNO-70). On the other hand, the pore volume of the SNO-15, SNO-30 and SNO-50 samples resulted higher, particularly for the former, with respect to those of the two bare components (SNO and CeO_2). This insight is very interesting, and it can justify the observed activity of these samples that however will be discussed in the next section 3.2. Anyhow, a decrease of the pore volume is observed in the composites by increasing the perovskite amount showing for the SNO70 sample the same value observed for the bare perovskite (see Table 2).

Concluding, among the composite materials, the sample with higher SSA and pore volume results to be SNO-15. It is worth to note that the pore size, measured by BJH desorption, and their distribution profiles indicated that all the materials have a mesoporous structure according to IUPAC classification.

The FTIR of the samples are reported in Fig. 5. The strong cut-off band observed below 550 cm^{-1} corresponds to the Ce-O stretching modes of the CeO_2 semiconductor [28]. The transition located at 864 cm^{-1} and those located at around 700 cm^{-1} can be attributed to the Sr-O and Sr-O-Sr stretching modes in the perovskite [29]. As it can be observed in Fig. 5, the intensity of these vibrational transition increases by increasing the amount of $SrNiO_3$ in the composite. The Ni-O transition attributable to Ni–O stretching band observed at 547 cm^{-1} for the bare perovskite [30], completely disappears in the composite materials because it overlaps with the large band observed for CeO_2 at wavenumbers below 600 cm^{-1}.

The optical properties of the samples were investigated by transforming the UV–Vis diffuse reflectance spectrum (DRS) of each sample in the corresponding Kubelka-Munk function, $F(R_\infty)$, used as the equivalent of absorbance. The band-gap values of all the samples has been estimated by extrapolating a linear fitting in the Tauc plot corresponding to the function ($[F(R_\infty) \bullet h\nu]^{1/2}$ versus the $h\nu$ values, assuming an indirect transition [31]. The Tauc-plots of all the composites materials are reported in Figs. 6 and 7. The experimental band-gap value of SNO shows energy absorption which over-laps the visible light spectrum of the solar irradiation (2.70 eV corresponding to ca. 440 nm) in agreement with previous reports [32]. On the other hand, the estimated band gap of bare CeO_2 was 3.18 eV. Instead, the bang-gap of the composite materials resulted to be intermediate between the band-gap values of the two components, namely SNO and CeO_2, probably due to the formation of a heterojunction between the two semiconductors or the formation of intermediate energy levels as before observed also with other materials [33,34]. Interestingly, this reduction of the band gap is more evident by increasing the amount of perovskite in the composite.

The study of the semiconducting proprieties of the elaborated materials as well as the investigation of their type n or p can be done by the Mott-Schottky measurement. The Mott-Schottky measurements of $SrNiO_3$ synthesized via the sol-gel, CeO_2 prepared by co-precipitation
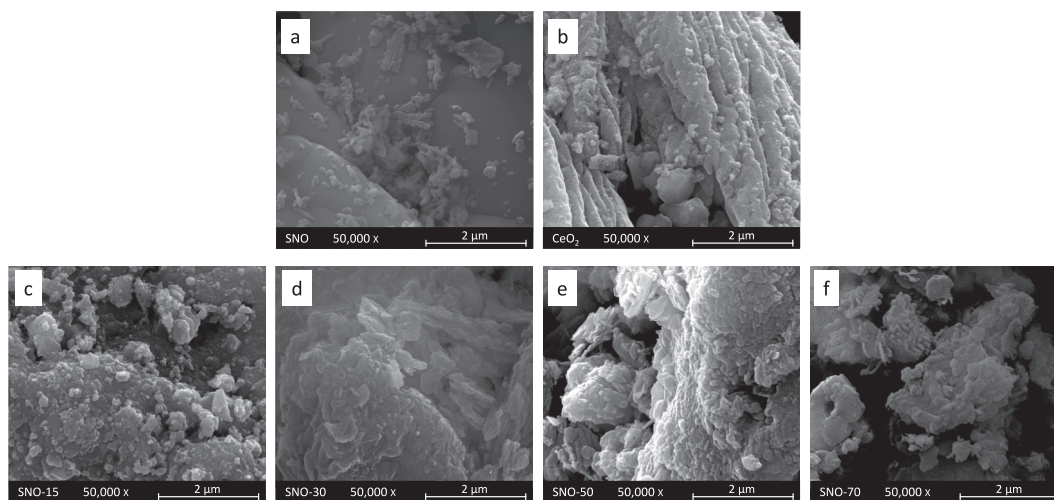

Fig. 3. SEM pictures of (a) SNO, (b) CeO_2, (c) SNO-15, (d) SNO-30, (e) SNO-50, and (f) SNO-70 samples at the same enlargement (50,000 X).

Table 2
Textural properties of the prepared materials.

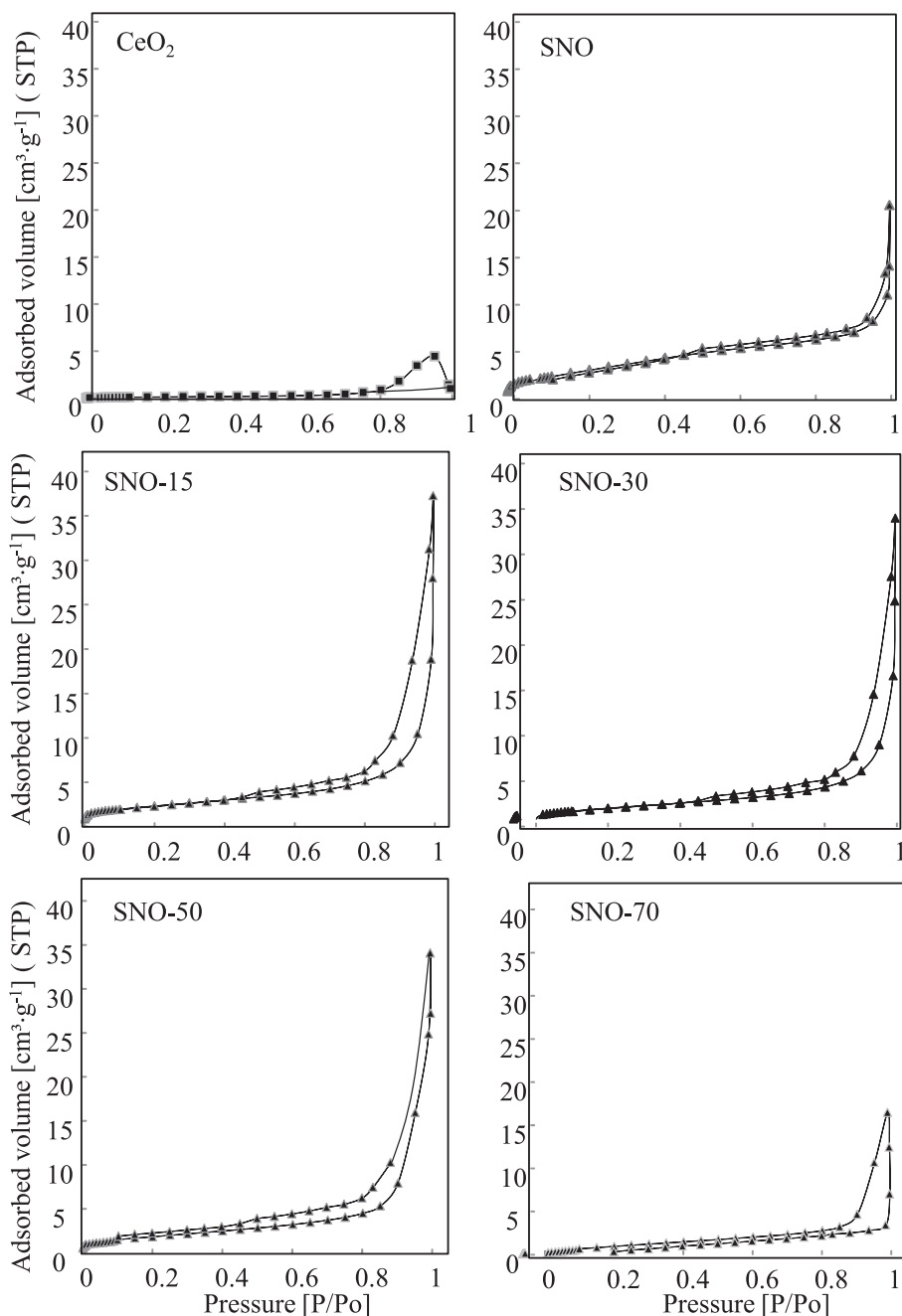| Sample	SSA ($m^2 \bullet g^{-1}$)	Pore Volume ($cm^3 \bullet g^{-1}$) by BJH des	Pore Size (nm) by BJH des
CeO_2	7.2	0.15	48
SNO	11.9	0.020	6.4
SNO-15	8.3	0.048	20
SNO-30	7.3	0.042	21
SNO-50	6.4	0.039	23
SNO-70	6.0	0.021	22

Fig. 4. N$_2$ adsorption–desorption isotherms of the bare CeO$_2$ and SrNiO$_3$ perovskite along with the composite materials.

method and the heterojunction between them (SNO-15, SNO-30, SNO-50, SNO-70). This electrochemical measurement is based on the formation of a Schottky barrier between the semiconductor and electrolytic bath [35]. As mentioned, the Mott Schottky method required calculating the capacitance of the space charge region (C$_{sc}$) in function of electrode tension. Equation (1) is based on measuring the capacitance of the space charge region (C$_{sc}$) versus the potential of the working electrode according to the relation [35–38].

$$\frac{1}{C_{SC}^2} = \frac{2}{\varepsilon \varepsilon_0 N_d S^2}\left(E - E_{fb} - \frac{KT}{e_0}\right) \tag{1}$$

where ε and N_d are the relative dielectric and the free carrier of the analyzed material, ε_0 is the space permittivity (8.85•10^{-14}F cm^{-1}), S is the area in contact with the electrolyte, E is the applied potential, E_{fb} is the flat band potential, K is the Boltzmann constant (1.38•10^{-23} J•k^{-1}),

T is the absolute temperature (298 K), and e_0 is the elementary charge of the electron. Fig. 8 presents the Mott-Schottky plots (1/C$_{SC}^2$ vs. E) of the synthesized CeO$_2$, SrNiO$_3$ and their composites SNO-15, SNO-30, SNO-50 and SNO-70.

The Mott-Schottky plots allowed to verify the nature (n or p) of the studied semiconductor material and find out its electronic properties, such as the density of the donor and acceptor charge carrier, and the flat band potential.

A perusal of Fig. 8 indicate that all the plots exhibit a positive slope meaning that the all samples belong to n-type semiconductor. Moreover, as we can see, all these plots show a very high slope with approximately the same value. This is an indication that the value of the free carrier concentration N$_d$ is very high for all the prepared materials. By assuming that the value of the relative dielectric does not change significantly by the change in the percentage of SrNiO$_3$ in the composite, it can be said
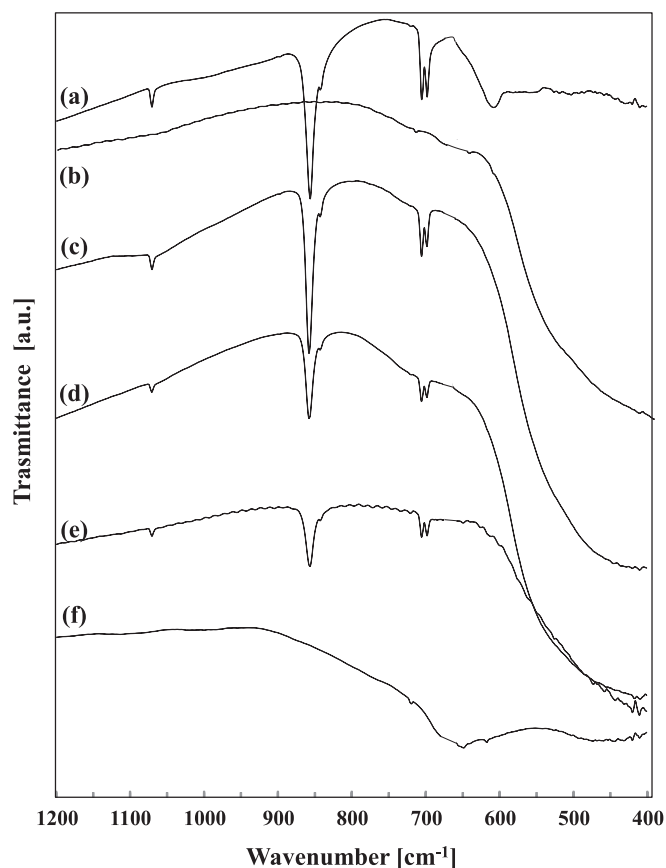
Fig. 5. FTIR spectra of the photocatalysts: (a) SNO; (b) CeO₂; (c) SNO-70; (d) SNO-50; (e) SNO-30; (f) SNO-15.

that the increase of the SrNiO₃ ratio in the composites does not change the free carrier concentration value N_d. The extrapolation of the linear part of the plot on the x-axis directly gives us the value of the flat band potential E_{fb}. As it is possible to see, the increase of the SrNiO₃ ratio in the synthesized composite leads to an increase of the negative value of the flat band potential.

Table 3 reports for all the prepared samples the value of the E_{fb} calculated and the type of semiconductor.

By approximating the E_{fb} to the potential of the conduction band E_{CB} it was possible (see table 3) to calculate the potential of the valence band E_{VB} as:

$$E_{VB} = E_{CB} + Egap \tag{2}$$

where Egap is the measured band gap. It is interesting to observe that the values of the E_{VB} of the composite materials decrease by increasing the percentage of the perovskite in the composites indicating that among them the higher oxidant ability is shown by the SNO-15 catalyst.

The Electrochemical Impedance Spectroscopy (EIS) was done by application of a sinusoidal perturbation (potential or current) over a large frequencies' domain. It permits the quantification of the bulk, grains boundaries and diffusion. The Nyquist plot in which the imaginary impedance (Z'') is diagrammed versus real impedance (Z') is reported in Fig. 9 for each samples studied.

The provided Nyquist plots depict the impedance spectra for the various semiconductor materials used. As general observations, the Nyquist plot exhibits semicircular arcs which are typical for electrochemical impedance spectra. The diameter of the semicircle is indicative of the charge transfer resistance (Rct), and a larger semicircle implies higher resistance. The inset graph shows the SNO-15 spectrum which highlighting its impedance at lower frequencies.

In order to make a comparison between the different prepared materials, CeO₂ has the largest semicircle, indicating the highest charge transfer resistance among the tested materials, SNO exhibits a relatively smaller semicircle compared to CeO₂, indicating a lower charge transfer resistance. The composite SNO-15, SNO-30, SNO-50 materials show smaller semicircles, indicating lower charge transfer resistances compared to CeO₂ and SNO and also to SNO-70. Among the all prepared samples, SNO-15 shows the smallest semicircle suggesting that it has the lowest charge transfer resistance, which is essential for efficient charge transfer [39,40] and consequently for photocatalytic reaction purpose.

3.2. Photocatalytic activity in gas–solid regime

3.2.1. 2-propanol photocatalytic oxidation under simulated solar light irradiation (SolarBox)

The photocatalytic activity of the samples was studied by a model reaction, i.e. the 2-propanol oxidation in gas–solid regime. The photoreactivity runs started after the reaching of the steady state conditions of the system under dark conditions. A time of half hour was enough for the substrate to be adsorbed on the photocatalysts surface. After the equilibration time, the initial substrate concentration, experimentally measured, was slightly lower than the nominal one (ca. 5 % for all the samples), indicating only a modest adsorption of 2-propanol on the catalyst surface. The contemporary presence of O₂, catalyst, and light was needed for the occurrence of 2-propanol degradation. Each photocatalytic experiment lasted six hours, being initiated once the Solar-Box apparatus was turned on. In literature, 2-propanol has been extensively
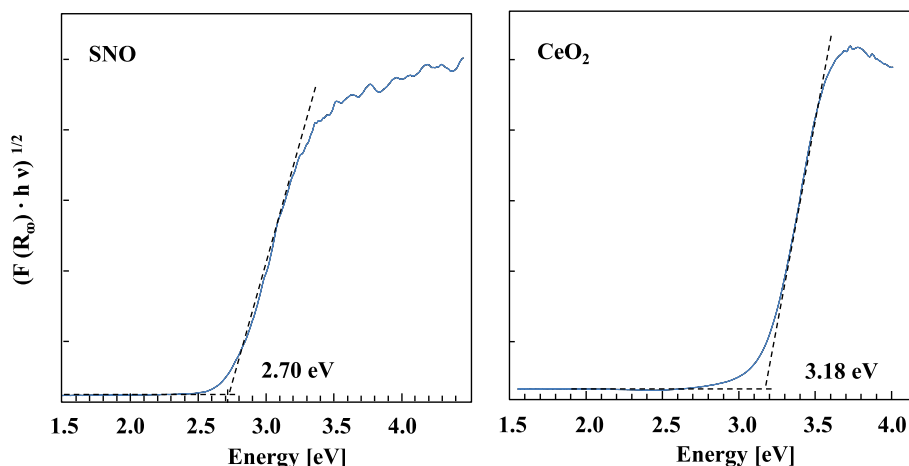

Fig. 6. Tauc plots of the bare SNO and CeO₂ photocatalysts.
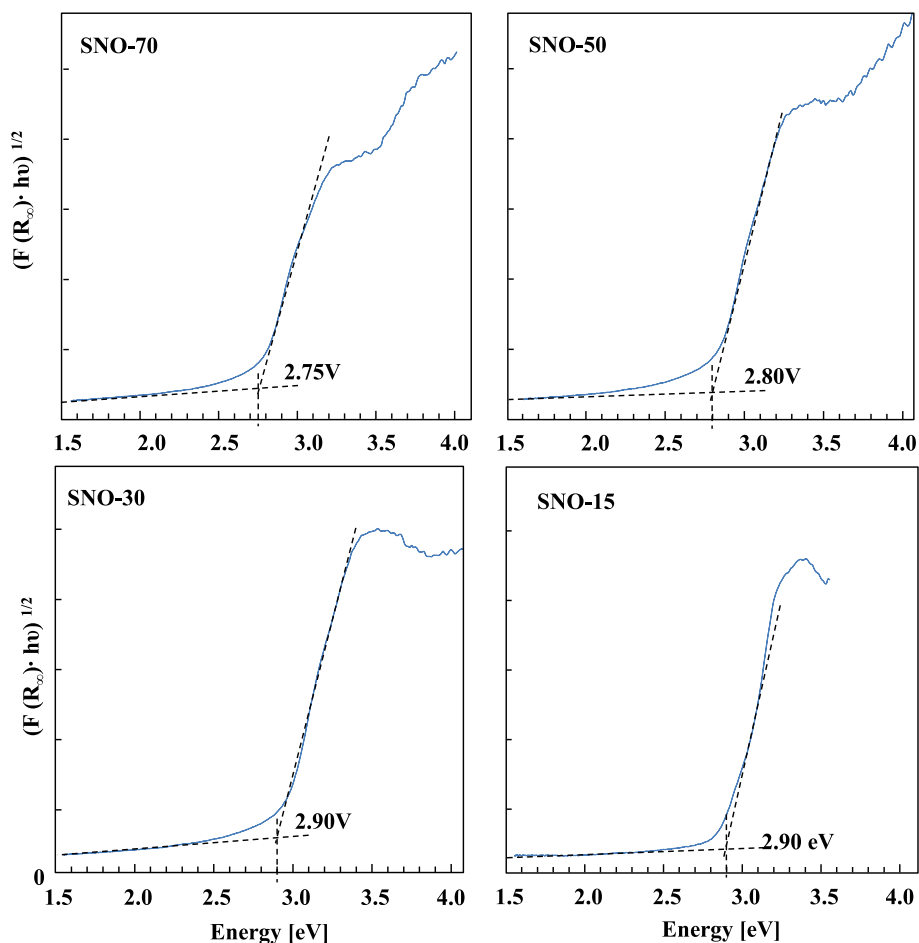
Fig. 7. Tauc plots of the composite photocatalysts.

used as a model molecule to evaluate the effectiveness of photocatalysts. Its photocatalytic oxidation typically gives rise to propanone and eventually CO_2 and H_2O when the substrate achieves its complete mineralization. The presence of acetaldehyde was also re-ported as intermediate depending on the photocatalysts and irradiation source used [32,41,42]. Moreover, strongly acidic sites can produce the dehydration of the substrate, producing propene and water as reaction byproducts [43].

The 2-propanol adsorption and decomposition, mainly studied on TiO_2 surfaces both in gas–solid [21,22] and in liquid–solid regimes [44–46], in both cases, proceed according to two pathways by either dehydrogenation or dehydration, giving rise to propanone or propene, respectively. The selectivity to these intermediate products strongly depends on the experimental conditions and particularly on the acid-base properties of the solid photocatalyst. In fact, it is suggested that dehydration of 2-propanol into propene results from the catalyst acidic character, whereas its dehydrogenation to propanone is due to its basicity [47,48]. In the current experiments, only propanone was observed.

Fig. 10 reports the concentrations of both 2-propanol and propanone vs. irradiation time for runs carried out in the presence of the bare SNO and CeO_2 samples. Under irradiation, an initial in-crease of the 2-prop-anol concentration, attributed to a photo/thermal desorption of the molecule, was observed. Hence, a certain degradation of the alcohol occurred, as proved by the formation of low amount of propanone. Beyond the desorption phenomena, the evolution of 2-propanol during the course of the reaction does not change significantly for the SNO material, indicating that the activity of this catalyst was very low. The CeO_2 photocatalyst was, instead, slightly more active with respect to

SNO giving rise a decrease of the concentration of the substrate with a contemporary formation of propanone (see Fig. 10). However, the concentration of propanone does not increase at the same rate as the concentration of 2-propanol decreases, indicating either a possible alternative route of oxidation of the substrate and/or to the adsorption of the intermediates on the catalysts surface.

Carbon dioxide was measured but no significant amount of mineralization of the model molecule was observed by using both bare solids (perovskite and CeO_2). Conversely, two of the four composite materials (SNO-15 and SNO-30) showed a significant decrease of the 2-propanol concentration with the irradiation time and contemporaneously an increase in the propanone concentration was observed along with CO_2 as the final oxidation product. The evolution of 2-propanol concentration as well as those of propanone and CO_2 for the run carried out in the presence of the composite samples is reported in Fig. 11.

The fastest 2-propanol degradation was observed in the presence of the SNO-15 photocatalyst. 2-propanol disappeared after ca. 5 h of irradiation, in the same run, propanone concentration increased, and its degradation began when the concentration of 2-propanol was almost zero. This behaviour suggests that the sites for the 2-propanol oxidation can be also useful for the propanone degradation. The activity of the composites decreases in the order: SNO-15 > SNO-30 > SNO-50 > SNO-70, so the lower the amount of perovskite, the higher the photocatalytic activity. A possible explanation of this occurrence is reported at the end of the next section which reports the study of the photocatalytic activity of all the samples under UV irradiation. Indeed, SNO-15 resulted still the most active in the photocatalytic degradation of 2-propanol also irradiating the system with UV-LED.

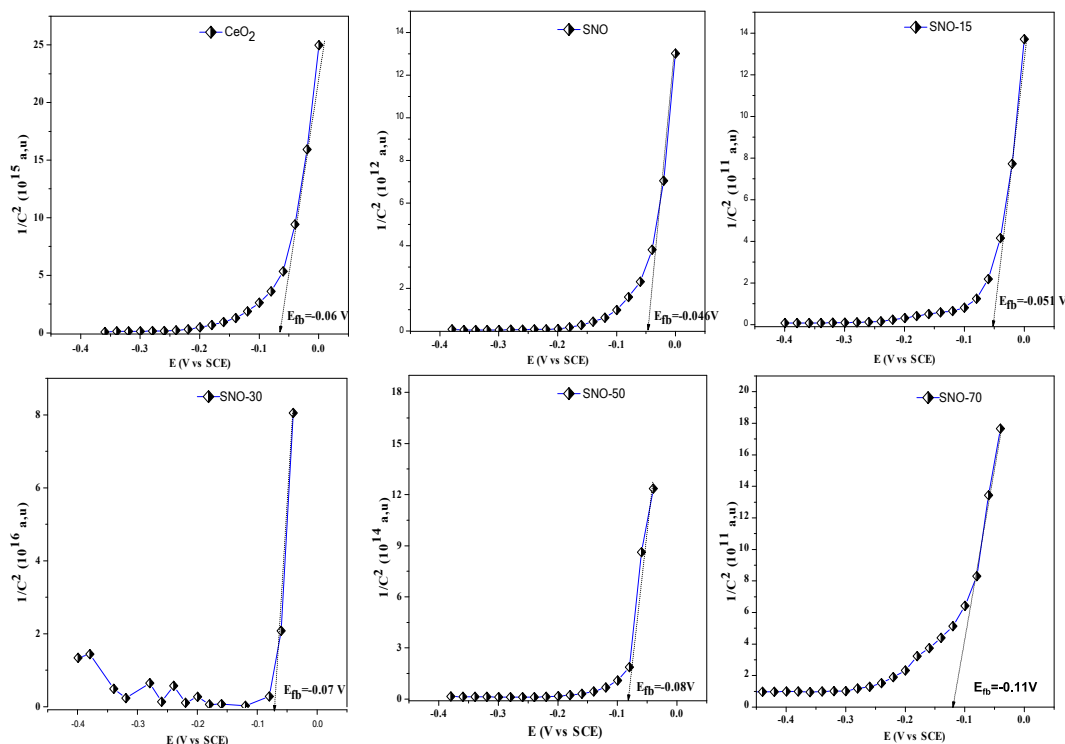According to Yamashita et al.[48] there are two routes in

Fig. 8. Mott–Schottky plots for CeO_2, $SrNiO_3$ and their composites SNO-15, SNO-30, SNO-50 and SNO-70 recorded in aqueous solution of KCl (1 M) with 0.2 kHz employed frequency.

Table 3
Electrochemical features of the prepared materials.

Sample	Type of semiconductor	E_{fb} (eV)	E_{VB} (eV)
SNO	n	−0.046	+2.65
CeO_2	n	−0.060	+3.12
SNO-15	n	−0.051	+2.85
SNO-30	n	−0.070	+2.83
SNO-50	n	−0.080	+2.72
SNO-70	n	−0.110	+2.65

photocatalytic oxidation of 2-propanol in gas solid regime, i.e., direct oxidation of 2-propanol to CO_2 and indirect oxidation of 2-propanol to CO_2 via acetone (schematised in Fig. 12). It would be possible to observe CO_2 in the early stages of the reaction, even if we have no observed it in this research. That CO_2 would be formed by the direct oxidation process [49]. On the other hand, 2-propanol molecules, adsorbed on the surface of the photocatalyst, decompose into acetone, which is ultimately oxidized to CO_2 [50] following the pathway schematised in Fig. 12. The photoexcited electrons generated on the photocatalyst surface by the promotion of electrons from the valence band to the conduction band are consumed via the two-electron reduction of O_2 to give H_2O_2, accompanied by the oxidation of 2-propanol to acetone via the two-electron oxidation:

$$CH_3CH(OH)CH_3 + 2h^+ \rightarrow CH_3COCH_3 + 2H^+ \qquad (3)$$
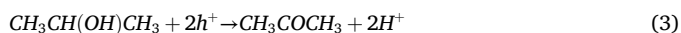
In Fig. 12 the presence of reactive oxidizing species (ROS) namely $^\bullet OH$, $^\bullet O^{2-}$, $^1O_2$ and h^+ formed during the photocatalytic reaction are the responsible of the oxidation.

3.2.2. 2-propanol photocatalytic oxidation in the presence of UV-LED irradiation

Further experiments of 2-propanol photocatalytic-oxidation were carried out by using the same reactor but irradiating the system with an UV-LED emitting at 365 nm. The results obtained are reported in Figs. 13

and 14 for bare and composite materials, respectively. The reaction lasted 2 h because it was much faster than that observed using simulated solar light due to the higher power of the UV irradiation source.

Both the bare materials, i.e. the perovskite and CeO_2 resulted active for the 2-propanol oxidation (see Fig. 13) being the CeO_2 slightly more active than the perovskite, also in this case. By comparing the results reported in Fig. 13 with those of Fig. 14, the composite materials resulted more active than the bare powders, at least those containing the lower amount of perovskite. These results confirmed that the SNO-15 composite is the most active sample in terms of 2-propanol oxidation also under UV irradiation.

Moreover, in the presence of this last photocatalyst a complete mineralization of 2-propanol was observed. Indeed, the amount of CO_2 formed during the reaction carried out under UV irradiation increased with the reaction time and its quantity, analysed after two hours, achieved the stoichiometric amount. At this time, both 2-propanol and propanone completely disappeared and only CO_2 was detected inside the reactor. Also, it is interesting to observe that in the presence of the SNO-15 material, the rate of propanone formation almost corresponds to that of the 2-propanol degradation. In order to compare the photoactivity of the different photocatalysts by using both the irradiation systems the conversion of the substrate at the end of the reaction a long with the initial reaction rate have been calculated and collected in Table 4.

The percentage of the conversion of 2-propanol, X, has been calculated as follows:

$$X = \frac{[2\text{-propanol}]_i - [2\text{-propanol}]}{[2\text{-propanol}]_i} \cdot 100 \qquad (1)$$

where $[2\text{-propanol}]_i$ represent the initial concentration of 2-propanol and $[2\text{-propanol}]$ the concentration of 2-propanol at the end of the reaction.

From the observation of the results collected in Table 4 it is evident that the SNO-15 sample is the catalyst with the best performance, likely due to the favourable combination of some factors. From the
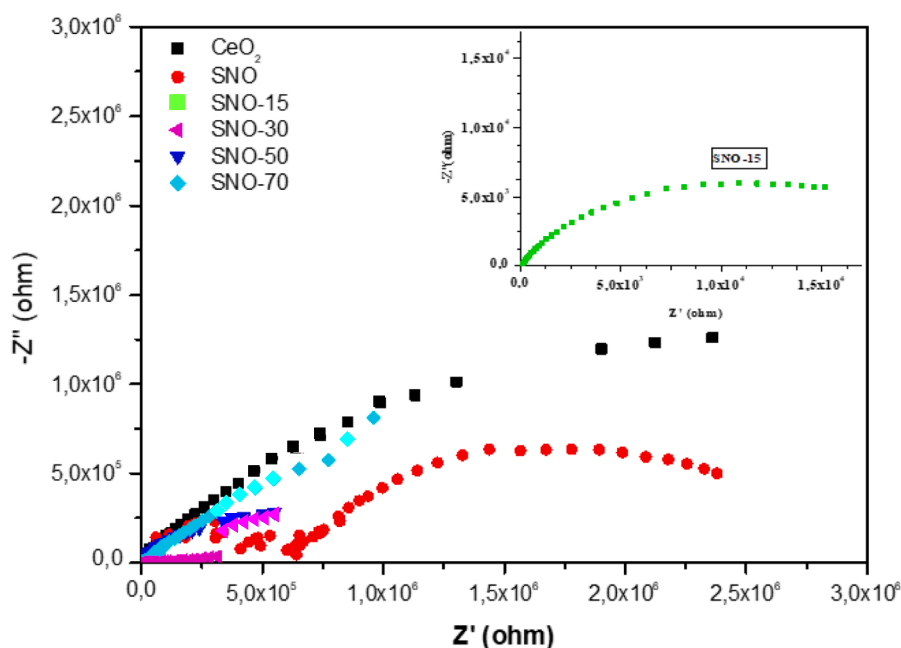
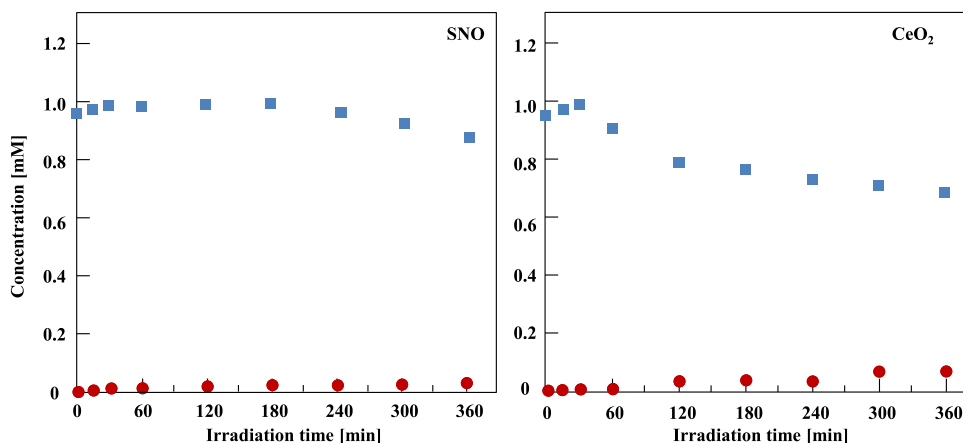**Fig. 9.** Nyquist plots of different samples in 1 M KCl solution.

Fig. 10. Evolution of 2-propanol (■) and propanone (●) concentrations vs. irradiation time for runs carried out in the in the presence of bare SrNiO$_3$ perovskite (SNO) and CeO$_2$ under simulated solar light irradiation (SolarBox).

characterization, it is possible to identify some distinctive characteristics of this material, like the strong interaction with CeO$_2$ highlighted by the XRD pattern that evidenced the presence of a distorted perovskite phase. This strong interaction from the two materials constituting the composites, i.e. SrNiO$_3$ and CeO$_2$, could hinder the recombination of the photoproduced electron-hole couples.

Furthermore, the SNO-15 sample showed, among the composite photocatalysts, the highest SSA and pore volume indicating a better accessibility of the substrate to the active sites of the catalyst. SNO-15 showed, moreover, a lower band gap than that of the bare ceria. The electrochemical characterization indicates, moreover that this sample presents the lowest charge transfer resistance in comparison to the other samples here studied. All of these features characterized the SNO-15 material, giving rise to an optimal photocatalytic activity of this photocatalyst.

Fig. 15 illustrates the band scheme of the composite materials, that after the UV light absorption allows electrons to be transferred from the highest occupied molecular orbital (HOMO) of the valence band to the lowest unoccupied molecular orbital (LUMO) of the conduction band in the semiconductors. This displacement of the electron generate a hole (h$^+$) that remained at the high oxidizing state. At the same time, the promoted electron possess the reductive property of the CB. By considering the energies of the CB and the VB of the two semiconductors, it can be hypothesized the formation of a Type I heterojunction as reported in Fig. 15. It is worth to remind that the photocatalytic active composite formed by two-phase semiconductors can be classified into three types of heterojunctions: Type-I (straddling gap), Type-II (staggered gap) and Type-III (broken gap) depending upon the interface structure of the semiconductor materials. [51]. The band gap scheme of the composite SNO-15, in Fig. 15, belongs to the Type-I heterojunction system where the conduction band bottom and valence band top of one of the semiconductors, here the perovskite, are located inside of the forbidden band of the other semiconductor material, in this present case the CeO$_2$. This allows the photogenerated electron-hole pairs produced in the CeO$_2$ to be transported into the SNO bands so improving the material performance. The presence of the type-I heterojunction has been observed to
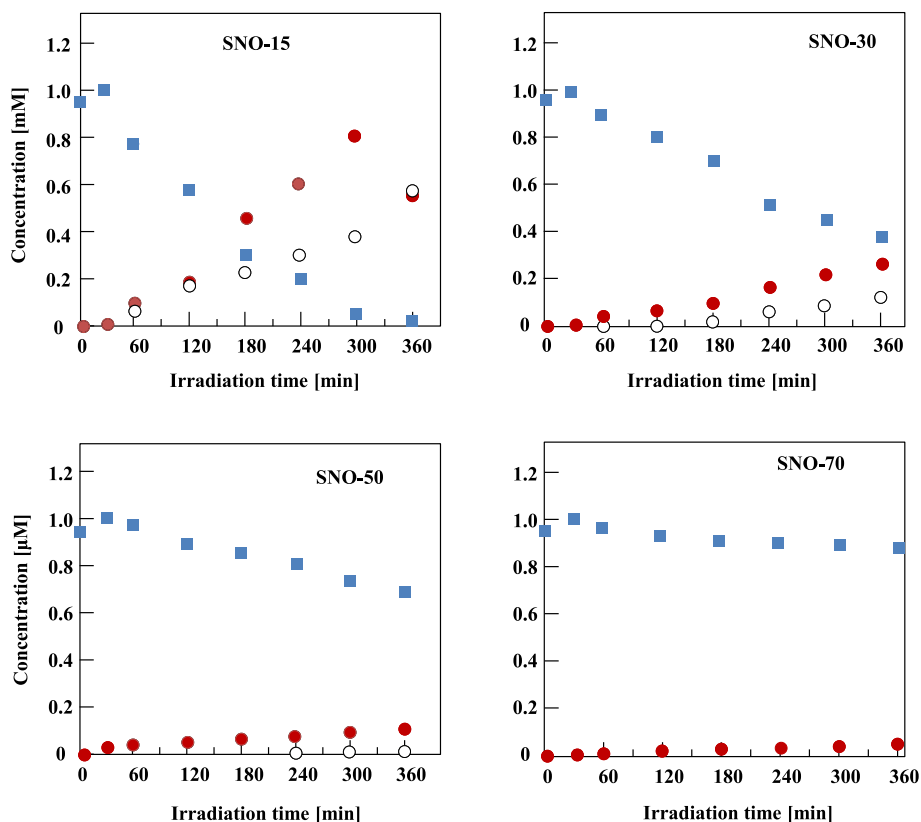
Fig.11. Evolution of 2-propanol (■), propanone (●) and CO₂ (○) concentrations vs. irradiation time for runs carried out in the presence of the composite photo-catalysts under simulated solar light irradiation (SolarBox).
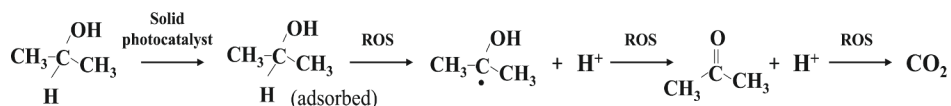

Fig. 12. Illustration of the reaction scheme of the 2-propanol oxidation by means of a heterogeneous photocatalytic process where the ROS (reactive oxygen species) are responsible for the oxidation of the organics to CO_2.
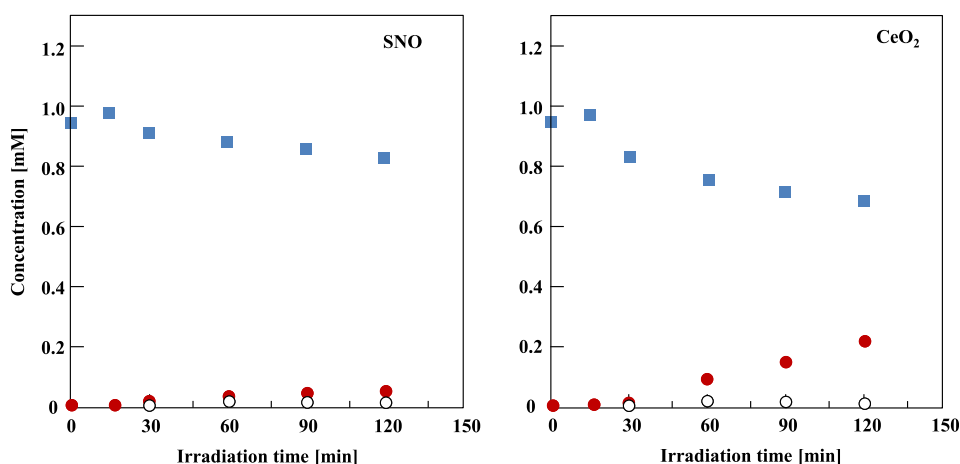

Fig. 13. Evolution of 2-propanol (■), propanone (●) and CO₂ (○) concentrations vs. irradiation time in the in the presence of $SrNiO_3$ perovskite (SNO) and CeO_2 under UV LED irradiation.

improve the activity of some composites acting as photocatalysts, for example, ZnO/Co_3O_4 [51], $g\text{-}C_3N_4/MgFe_2O_4$ [52] or $CuO/BaTiO_3$ [53].

Therefore, after the formation of the electron-hole pairs in both structures, the holes in the VB of CeO_2 structure can be transferred to the VB of $SrNiO_3$ and the electron promoted in the CB of the first can be transferred in the CB of $SrNiO_3$. The positive impact of the hetero-junction formed, particularly on SNO-15, can be ascribed to the mobility of the photogenerated carriers, that can increase the number of reactive
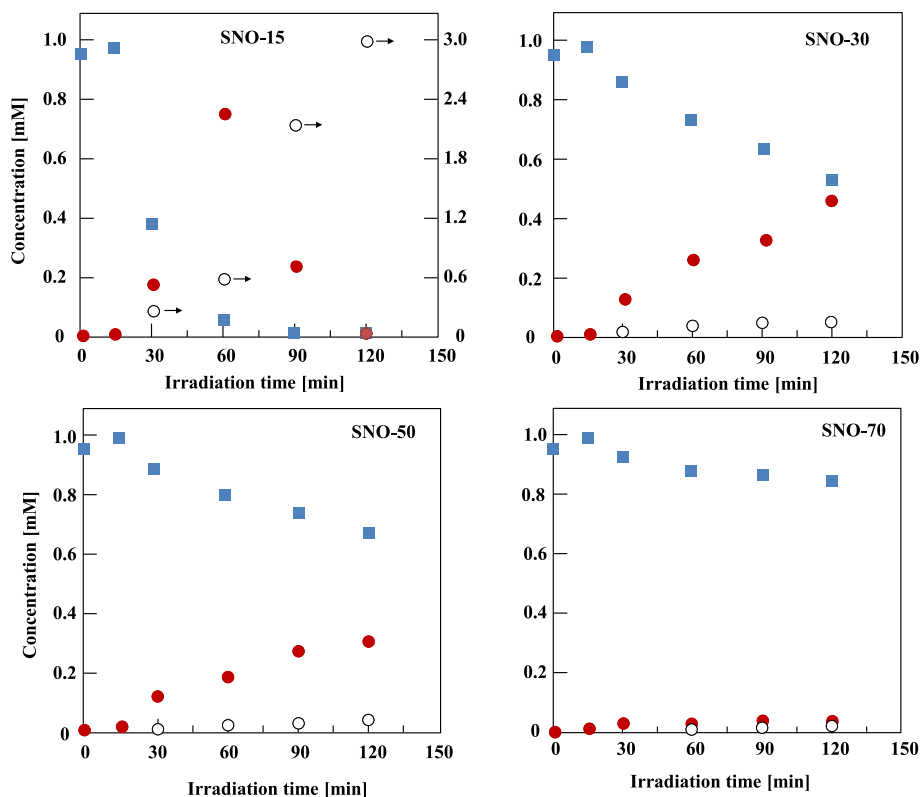
Fig. 14. Evolution of 2-propanol (■), propanone (●) and CO_2 (○) concentrations vs. irradiation time for runs carried out in the presence of the composite photocatalysts under UV LED irradiation.

Table 4

2-propanol conversion (X) after 6 h (SolarBox) or 2 h (UV-LED) of reaction and initial reaction rate (r_o) of 2-propanol heterogeneous photocatalytic oxidation by using the two sep-ups.

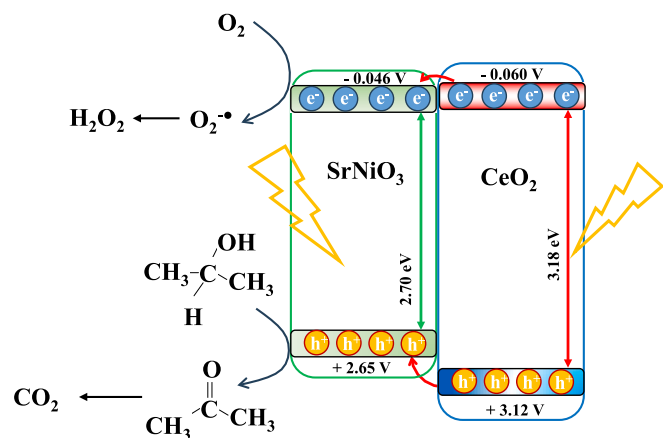| Sample	SolarBox X [%]	$r_o \cdot 10^3$ [mM·min^{-1}]	UV-LED X [%]	$r_o \cdot 10^3$ [mM·min^{-1}]
$SrNiO_3$	10	0.5	18	6.5
CeO_2	30	3.0	32	12.5
SNO-15	100	7.3	100	40.0
SNO-30	60	3.0	45	12.5
SNO-50	31	0.8	32	7.2

Fig. 15. Proposed working mechanism upon irradiation of the $SrNiO_3$-CeO_2 composite containing 15 % of perovskite (SNO-15).

events of the electron-hole pairs with O_2 and 2-propanol molecules, respectively on the surface of the photocatalyst.

Finaly, it can be interesting to compare the results obtained in this research with some other obtained with alternative materials in similar conditions, indeed it can be mentioned that various semiconductors have been tested in almost the same conditions, and the results have been previously reported by us. In particular, Nb_2O_5 home prepared, both bare and its composites with TiO_2, CeO_2 and ZrO_2 [54]; as well as ZrO_2 and Ce and Er-doped ZrO_2 [55] resulted photoactive in gas–solid regime for 2-propanol photooxidation to propanone by using the SOLARBOX as irradiating source.

The initial reaction rate of 2-propanol oxidation obtained in the current research, in the presence of SNO-15 resulted 7.3 10^{-3} mM min^{-1}, whereas the best material based on Nb_2O_5, the Nb_2O_5-TiO_2 composite [54], gave rise to an initial reaction rate of ca. one order of magnitude higher than SNO-15. On the contrary, the best performant ZrO_2 based material, i.e., ZrO_2 doped with a 10 % of Ce [55], showed an initial 2-propanol oxidation rate of ca. five orders of magnitude lower than that obtained in the presence of the SNO-15.

4. Conclusions

Perovskites have demonstrated great potential in catalysis and photocatalysis due to their unique properties as specific surface area morphology and shape of particles. In the present work, a CeO_2 material has been enriched with the perovskite $SrNiO_3$ with different percentages from 15 to 70 % in mass. Both perovskite and ceria were prepared and then the composite obtained by ball milling. All the obtained materials were used as heterogeneous photocatalysts for the 2-propanol oxidation in gas–solid regime by irradiating the system with simulated solar light or by an UV-LED. The photocatalytic results suggest that the photocatalyst containing a 15 % of $SrNiO_3$ perovskite is the most active, and the activity decreases by increasing the perovskite content in the

$SrNiO_3$/ CeO_2 composites. The pristine $SrNiO_3$ material showed negligible photocatalytic activity, whereas the CeO_2 showed some activity. The presence of a small amount of $SrNiO_3$ improves the 2-propanol oxidation with respect to the bare ceria both by irradiating the photocatalyst with simulated solar light irradiation or by UV. The highest activity showed by the SNO-15 sample was justified by considering for this sample a sum of favourable factors such as a strong interaction between $SrNiO_3$ perovskite and CeO_2 and the higher SSA and pore volume with respect to those of all the other composites as well as the lowest charge transfer resistance and the lowest band gap revealed in comparison to that of CeO_2.

CRediT authorship contribution statement

N. Aoun: Writing – original draft, Methodology, Investigation. **E.I. García-López:** Writing – review & editing, Writing – original draft, Visualization, Validation, Supervision, Methodology, Investigation, Formal analysis, Data curation, Conceptualization. **H. Boucheloukh:** Visualization, Methodology, Funding acquisition, Conceptualization. **M. Boulekroune:** Investigation. **T. Sehili:** Resources, Methodology, Funding acquisition, Conceptualization. **G. Marcì:** Writing – review & editing, Visualization, Validation, Supervision, Resources, Project administration, Methodology, Investigation, Funding acquisition, Formal analysis, Data curation, Conceptualization.

Declaration of competing interest

The authors declare that they have no known competing financial interests or personal relationships that could have appeared to influence the work reported in this paper.

Data availability

Data will be made available on request.

Acknowledgement

References

[1] E.I. García-López, L. Palmisano (Eds.), Materials Science in Photocatalysis, 1st Ed., Elsevier, Amsterdam, 2021.

[2] Z.W.F. Polo-Garzon, Acide-Base Catalysis over Perovskites: A Review, J. Mater. Chem. A. (2018) 2877–2894.

[3] E. Grabowska, Selected perovskite oxides: characterization, preparation and photocatalytic properties-a review, Appl. Catal. B Environ. 186 (2016) 97–126.

[4] H. Wang, Q. Zhang, M. Qiu, B. Hu, Synthesis and application of perovskite-based photocatalysts in environmental remediation: a review, J. Mol. Liq. 334 (2021) 116029.

[5] J.P. Correa-Baena, M. Saliba, T. Buonassisi, M. Grätzel, A. Abate, A. Tress, A. Hagfeldt, Promises and challenges of perovskite solar cells, Science 358 (2017) 739–744.

[6] W.J. Yin, B. Weng, J. Ge, Q. Sun, Z. Li, Y. Yan, Oxide perovskites, double perovskites and derivatives for electrocatalysis, photocatalysis, and photovoltaics, Energy Environ. Sci. 12 (2019) 442–462.

[7] J. Junita, D. Jayalakshmi, J.D. Rodney, Effect of annealing temperature on the bifunctional electrocatalytic properties of strontium nickelate (SrNiO₃) nanoparticles for efficient overall water splitting, Int. J. Hydrog. Energy. 47 (2022) 30602–30612.

[8] N. Ahmad, F. Alharthi, M. Alam, R. Wahab, S. Manoharadas, B. Alrayes, Syngas production via CO₂ reforming of methane over SrNiO₃ and CeNiO₃ perovskites, Energies 14 (2021) 2928.

[9] N. Aoun, H. Boucheloukh, K. Harrouche, B. Boughrara, SrNiO₃ perovskite synthesis for enhanced photodegradation of the nonsteroidal anti-inflammatory drug naproxen: a clean and sustainable process for water treatment, Inorg. Chem. Commun. 158 (2023) 111459.

[10] E. Cho, K. Klyukin, S. Ning, J. Li, R. Comin, R.J. Green, B. Yildiz, C.A. Ross, First-principles calculation of oxygen vacancy effects on the magnetic properties of the perovskite, Phys. Rev. Mater. 5 (2021) 094413.

[11] E. Ksepko, Perovskite-Type Sr(Mn₁₋ₓNiₓ)O₃ materials and their chemical-looping oxygen transfer properties, Int. J. Hydrogen Energy 39 (2014) 8126–8137.

[12] R. Gottschall, R. Schöllhorn, M. Muhler, N. Jansen, D. Walcher, P. Gütlich, Electronic state of nickel in barium nickel oxide, BaNiO₃, Inorg. Chem. 37 (1998) 1513–1518.

[13] Y. Takeda, T. Hashino, Y. Miyamoto, F. Kanamaru, S. Kume, M. Koizumi, Synthesis of SrNiO₃ and related compound, J. Inorg. Nucl. Chem. 34 (1972) 1599–1601.

[14] M. Zinkevich, Constitution of the Sr–Ni–O system, J. Solid State Chem. 178 (2005) 2818–2824.

[15] J. Lee, G.F. Holland, Identification of a New strontium Ni(III) Oxide prepared in molten hydroxides, J. Solid State Chem. 93 (1991) 267–271.

[16] T. Montini, M. Melchionna, M. Monai, P. Fornasiero, Fundamentals and catalytic applications of CeO₂-based materials, Chem. Rev. 116 (2016) 5987–6041.

[17] E.I. García-López, Z. Abbasi, F. Parrino, V. La Parola, L.F. Liotta, G. Marcì, Au/CeO₂ photocatalyst for the selective oxidation of aromatic alcohols in water under Uv, Visible and Solar Irradiation, Catalysts 11 (2021) 1467.

[18] M.S.P. Sudhakaran, M.M. Hossain, G. Gnanasekaran, Y.S. Mok, Dry Reforming of propane over γ-Al₂O₃ and nickel foam supported novel SrNiO₃ perovskite catalyst, Catalysts 9 (2019) 68.

[19] J. Peral, D. Ollis, Heterogeneous photocatalytic oxidation of gas-phase organics for air purification: acetone, 1-butanol, butyraldehyde, formaldehyde, and m-xylene oxidation, J. Catal. 136 (1992) 554–565.

[20] J. Gunschera, J.R. Andersen, N. Schulz, T. Salthammer, Surface-catalysed reactions on pollutant-removing building products for indoor use", Chemosphere 75 (2009) 476–482.

[21] R.I. Bickley, G. Munuera, F.S. Stone, Photoadsorption and photocatalysis at rutile surfaces: II. Photocatalytic oxidation of isopropanol, J. Catal. 31 (1973) 398–407.

[22] S.A. Larson, J.A. Widengree, J. Falconer, Transient studies of 2-propanol photocatalytic oxidation on Titania, J. Catal. 157 (1995) 611–625.

[23] F. Arsac, D. Bianchi, J.M. Chovelon, C. Ferronato, J.M. Herrmann, Experimental microkinetic approach of the photocatalytic oxidation of isopropyl alcohol on TiO₂. Part 1. Surface elementary steps involving gaseous and adsorbed C3HxO species, J. Phys. Chem. A 110 (2006) 4202–4212.

[24] N. Aoun, H. Boucheloukh, H. Belkhalfa, K. Harrouche, K. Boughrara, T. Sehili, Combined action of cerianite, UV and direct sunlight irradiation for the removal of violet crystal and methylene blue from aqueous solution, React. Kinet. Mech. Catal. 136 (2023) 1607–1623.

[25] G. Marcì, E.I. García-López, L. Palmisano, Photocatalytic CO₂ reduction in gas-solid regime in the presence of H₂O by Using GaP/TiO₂ composite as photocatalyst under simulated solar light, Catal. Commun. 53 (2014) 38–41.

[26] M. Guo, C. Guo, L. Jin, Y. Wang, J. Lu, M. Luo, Nano-Sized CeO₂ with extra-high surface area and its activity for CO oxidation, Mater. Lett. 64 (2010) 1638–1640.

[27] N. Yang, X. Zhang, L. Reynolds, D. Kumah, C. Xu, The Role of carbon content: a comparison of the nickel particle size and magnetic property of nickel/polysiloxane-derived silicon oxycarbide, Adv. Eng. Mater. 25 (2023) 2201453.

[28] M. Zarinkamar, M. Farahmandjou, T.P. Firoozabadi, One-step synthesis of ceria (CeO₂) nano-spheres by a simple wet chemical method, J. Ceram. Process. Res. 17 (2016) 166–169.

[29] P.A. Murade, V.S. Sangawar, G.N. Chaudhari, V.D. Kapse, A.U. Bajpeyee, Acetone gas-sensing performance of Sr-doped nanostructured LaFeO₃ semiconductor prepared by citrate sol-gel route, Curr. Appl. Phys. 11 (2011) 451–456.

[30] K. Rida, M.A. Peña, E. Sastre, A. Martinez-Arias, Effect of calcination temperature on structural properties and catalytic activity in oxidation reactions of LaNiO₃ perovskite prepared by Pechini method, J. Rare Earths 30 (2012) 210–216.

[31] J. Tauc, Absorption edge and internal electric fields in amorphous semiconductors, Mater. Res. Bull. 5 (1970) 721–729.

[32] E.I. García-López, G. Marcì, B. Megna, F. Parisi, L. Armelao, A. Trovarelli, M. Boaro, L. Palmisano, SrTiO₃-based perovskites: preparation, characterization and photocatalytic activity in gas-solid regime under simulated solar irradiation, J. Catal. 321 (2015) 13–22.

[33] O. Alduhaish, A. Kumar, P. Dhiman, M. Shekh, J. Sharma, G. Sharma, Integrating AgFeO₂ and Bi₅O₇I to establish an S-scheme heterojunction with significantly boosted norfloxacin photocatalytic degradation, J. Photochem. Photobiol. A 456 (2024) 115835.

[34] Z. Redouane-Salah, M. Boulahbal, Ö. Tuna, Z. Balta, E.B. Simsek, Construction of Z-scheme FeTiO₃/g-C₃N₄ heterojunction system: Characterization and statistical optimization of photocatalytic behavior under visible light irradiation, J. . Photochem. Photobiol. A, 446 (2024) 115185.

[35] J. Rousset, E. Saucedo, D. Lincot, Extrinsic doping of electrodeposited zinc oxide films by chlorine for transparent conductive oxide applications, Chem Mater 21 (2009) 534–540.

[36] C.F. Windisch, G.J. Exarhos, Mott-Schottky analysis of thin ZnO films, J Vac. Sci. Technol. 18 (2000) 1677–1680.

[37] I. Mora-Sero, F. Fabregat-Santiago, B. Denier, J. Bisquert, R. Tena-Zaera, J. Elias, C. Levy-Clement, Determination of carrier density of ZnO nanowires by electrochemical techniques, Appl. Phys. Lett. 89 (2006) 203117–203119.

[38] S.R. Morrison, Electrochemistry at semiconductor and oxidized metal electrodes, Plenum Press, New York, 1990.

[39] K. Wangkawong, S. Phanichphant, D. Tantraviwat, B. Inceesungvorn, Photocatalytic benzylamine efficiency improvement of Z-scheme CeO₂/BiOI heterostructure for RHB degradation and oxidation under visible light irradiation, J. Taiwan Inst. Chem. Eng. 108 (2020) 55–63.

[40] J. Shen, J. Shen, W. Zhang, X. Yu, H. Tang, M. Zhang, X. Zulfiqar, Q. Liu, Built-in electric field induced CeO₂/Ti₃C₂-MXene Schottky-junction for coupled photocatalytic tetracycline degradation and CO₂ reduction, Ceram. Int. 45 (2019) 24146–24153.

[41] E.I. García-López, G. Marcì, F. Puleo, V. La Parola, L.F. Liotta, La$_{1-x}$Sr$_x$Co$_{1-y}$Fe$_y$O$_{3-d}$ perovskites: preparation, characterization and solar photocatalytic activity, Appl. Catal. B Environ. 178 (2015) 218–225.

[42] F. Parrino, E.I. García-Lopez, G. Marcì, L. Palmisano, V. Felice, I. Natali Sora, L. Armelao, Cu-substituted lanthanum ferrite perovskites: preparation, characterization and photocatalytic activity in gas-solid regime under simulated solar light irradiation, J. Alloy. Comp. 682 (2016) 686–694.

[43] G. Marcì, E.I. García-López, L. Palmisano, Photo-assisted degradation of 2-propanol in gas-solid regime by using TiO$_2$ impregnated with heteropolyacid $_H$3P$_{W1}$2$_{O4}$0, Catal. Today 144 (2009) 42–47.

[44] B. Othani, K. Iwai, S. Nishimoto, S. Sato, J. Phys. Chem. B 101 (1997) 3349.

[45] A. Sclafani, J. Herrmann, J. Photochem. Photobiol. A: Chem. 113 (1998) 181.

[46] G. Marcì, E. García-López, G. Mele, L. Palmisano, G. Dyrda, R. Słota, Comparison of the photocatalytic degradation of 2-propanol in gas–solid and liquid-solid systems by using TiO$_2$–LnPc$_2$ hybrid powders, Catal. Today 143 (2009) 203–210.

[47] A. Gervassini, Y. Fenyvesi, A. Auroux, Catal. Lett. 43 (1997) 219.

[48] H. Yamashita, M. Honda, M. Harada, Y. Ichihashi, M. Anpo, T. Hirao, N. Itoh, N. Iwamoto, Preparation of titanium oxide photocatalysts anchored on porous silica glass by a metal ion-implantation method and their photocatalytic reactivities for the degradation of 2-propanol diluted in water, J. Phys. Chem. B 102 (1998) 10707–10711.

[49] S.C. Turich, F.D. Ollis, Photocatalytic degradation of organic water contaminants: mechanisms involving hydroxyl radical attack, J. Catal. 122 (1990) 178–192.

[50] O. Tomita, T. Otsubo, M. Higashi, B. Ohtani, R. Abe, Partial oxidation of alcohols on visible-light-responsive WO$_3$ photocatalysts loaded with palladium oxide cocatalyst, ACS Catal. 6 (2016) 1134–1144.

[51] C. Wang, H. Ni, J. Dai, T. Liu, Z. Wu, X. Chen, Z. Dong, J. Qian, Z. Wu, Chem. Comparison of highly active Type-I and Type-II heterojunction photocatalytic composites synthesized by electrospinning for humic acid degradation, Phys. Lett. 803 (2022) 139815.

[52] J. Chen, D. Zhao, Z. Diao, M. Wang, L. Guo, S. Shen, Bifunctional modification of graphitic carbon nitride with MgFe2O4 for enhanced photocatalytic hydrogen generation, Appl. Mater. Interf. 7 (2015) 18843–18848.

[53] S. Joshi, R.K. Canjeevaram Balasubramanyam, S.J. Ippolito, Y.M. Sabri, A. E. Kandjani, S.K. Bhargava, M.V. Sunkara, Straddled band aligned CuO/BaTiO$_3$ heterostructures: role of energetics at nanointerface in improving photocatalytic and CO$_2$ sensing performance, ACS Appl. Nano Mater. 1 (2018) 3375–3388.

[54] E.I. García-López, I. Krivtsov, S. Villar-Rodil, J.I. Paredes, G. Marcì, Nb$_2$O$_5$ and Nb based oxides as redox photocatalysts: partial oxidation of 2-propanol and H$_2$ generation by photoreforming, Mol. Catal. 558 (2024) 114010.

[55] E.I. García-López, G. Marcì, F.R. Pomilla, M.C. Paganini, C. Gionco, E. Giamello, L. Palmisano, ZrO$_2$ Based materials as photocatalysts for 2-propanol oxidation by using UV and solar light irradiation and tests for CO$_2$ reduction, Catal. Today 313 (2018) 100–105.